Journal of Energy Chemistry 58 (2021) 586–592

Contents lists available at ScienceDirect

Journal of Energy Chemistry

journal homepage: www.elsevier.com/locate/jechem

http://www.journals.elsevier.com/journal-of-energy-chemistry/

Structural properties and electrochemical performance of different polymorphs of Nb_2O_5 in magnesium-based batteries

Cunyuan Pei [a], Yameng Yin [a], Xiaobin Liao [a,b], Fangyu Xiong [a], Qinyou An [a,c,*], Mengda Jin [a], Yan Zhao [b,*], Liqiang Mai [a,c,*]

[a] State Key Laboratory of Advanced Technology for Materials Synthesis and Processing, Wuhan University of Technology, Wuhan 430070, Hubei, China
[b] State Key Laboratory of Silicate Materials for Architectures, International School of Materials Science and Engineering, Wuhan University of Technology, Wuhan 430070, Hubei, China
[c] Foshan Xianhu Laboratory of the Advanced Energy Science and Technology Guangdong Laboratory, Xianhu Hydrogen Valley, Foshan 528200, Guangdong, China

ARTICLE INFO

Article history:
Received 12 July 2020
Revised 27 October 2020
Accepted 27 October 2020
Available online 9 November 2020

Keywords:
Crystal structure
Nb_2O_5
Mg-ion storage
Li-ion storage
Diffusion kinetics

ABSTRACT

The selection of the most suitable crystal structure for ions storage and the investigation of the corresponding reaction mechanism is still an ongoing challenge for the development of Mg-based batteries. In this article, high flexible graphene network supporting different crystal structures of Nb_2O_5 (TT-Nb_2O_5@rGO and T-Nb_2O_5@rGO) are successfully synthesized by a spray-drying-assisted approach. The three-dimensional graphene framework provides high conductivity and avoids the aggregation of Nb_2O_5 nanoparticles. When employed as electrode materials for energy storage applications, TT-Nb_2O_5 delivers a higher discharge capacity of 129.5 mAh g^{-1}, about twice that of T-Nb_2O_5 for Mg-storage, whereas, T-Nb_2O_5 delivers a much higher capacity (162 mAh g^{-1}) compared with TT-Nb_2O_5 (129 mAh g^{-1}) for Li-storage. Detailed investigations reveal the Mg intercalation mechanism and lower Mg^{2+} migration barriers, faster Mg^{2+} diffusion kinetics of TT-Nb_2O_5 as cathode material for Mg-storage, and the faster Li^+ diffusion kinetics, shorter diffusion distance of T-Nb_2O_5 as cathode material for Li-storage. Our work demonstrates that exploring the proper crystal structure of Nb_2O_5 for different ions storage is necessary.

1. Introduction

Lithium-ion batteries (LIBs) are widely used as an advanced energy storage system to support emerging portable electronics [1,2]. But the further applications of LIBs are hindered by the safety issues and high cost [3]. Rechargeable magnesium-based batteries are promising alternatives owing to the low cost, high volumetric capacity, and dendrite-free plating (in specific conditions) of Mg [4–6]. Despite these advantages, the development of magnesium-based batteries is impeded by several key technical issues, such as the incompatibility of Mg metal anode with most of the conventional electrolytes and the sluggish solid-state diffusion kinetics of divalent Mg^{2+} in host structures [7–9]. Therefore, developing new cathodes for high-performance Mg-based batteries is a challenging, but necessary research direction.

In an effort to explore host materials for reversible storage of Mg^{2+}, some materials with diverse phase structures have shown an obvious difference in Mg storage performance. Nazar et al. have extensively investigated the layered TiS_2 and thiospinel Ti_2S_4 as cathode materials in magnesium batteries. The thiospinel Ti_2S_4 exhibits much higher discharge capacity, working voltage, and cycling stability than that of layered TiS_2 [10,11]. The superior electrochemical performance of thiospinel Ti_2S_4 can be attributed to the lower Mg migration barriers in thiospinel Ti_2S_4 (~800 meV) than that of layered TiS_2 (~1200 meV) [12]. In addition, different forms of V_2O_5 polymorphs (α-V_2O_5 and δ-V_2O_5) were also widely studied as host materials for Mg-ion storage [13–17]. The density functional theory (DFT) calculations suggest that δ-V_2O_5 possesses much lower migration barriers, larger layer spacing, and smaller coordination changes than those of α-V_2O_5, indicating δ-V_2O_5 is a more desirable host material for Mg^{2+} [14,18,19]. However, experimental results show that δ-V_2O_5 has a much lower Mg insertion level of about 0.17, and the layered α-V_2O_5 structure can accommodate as high as 0.5 Mg^{2+} for per formula V_2O_5 [13,15]. The above examples indicate that the intrinsic crystal structure of specific electrode materials has a significant influence on battery performance. Recently, various polymorphic forms of Nb_2O_5 (such as

* Corresponding authors at: State Key Laboratory of Advanced Technology for Materials Synthesis and Processing, Wuhan University of Technology, Wuhan 430070, Hubei, China (L. Mai).
E-mail addresses: anqinyou86@whut.edu.cn (Q. An), yan2000@whut.edu.cn (Y. Zhao), mlq518@whut.edu.cn (L. Mai).

https://doi.org/10.1016/j.jechem.2020.10.033

TT-, T-, and H-Nb_2O_5) have been frequently synthesized and introduced as electrode materials for alkali-ion batteries, which display acceptable discharge capacities and high-rate capabilities [20–27]. Among them, the T-Nb_2O_5 exhibits an exceptionally enhanced rate performance and remarkable cycling stability than that of other forms, and the detailed Li^+/Na^+ ions storage mechanism has been revealed. Different structures of Nb_2O_5 may exhibit different electrochemical behaviors when employed as host materials for energy storage applications. Therefore, it is necessary to explore the promising phase structure as well as the corresponding ion storage mechanism of Nb_2O_5 for high-performance Mg-based batteries.

In the present work, we designed and constructed three-dimensional reduced graphene oxide (rGO) framework encapsulating two different phases of Nb_2O_5, namely, TT-Nb_2O_5@rGO (pseudohexagonal phase) and T-Nb_2O_5@rGO (orthorhombic phase), through a scalable spray-drying method and subsequent calcination process. The three-dimensional rGO network can not only avoid the agglomeration of Nb_2O_5 nanoparticles but also offer a fast ion/electron diffusion route. The effect of crystal structures on Mg-ion and Li-ion storage performance was systematically investigated. Interestingly, TT-Nb_2O_5@rGO displays much better electrochemical performance in $Mg[N(SO_2CF_3)_2]_2$/dimethoxyethane ($Mg(TFSI)_2$/DME) electrolyte, whereas, T-Nb_2O_5@rGO displays much better electrochemical performance in Mg-Li dual salt electrolyte. The intrinsic difference between Mg^{2+} and Li^+ solid-state diffusion kinetics in the two phases was studied via galvanostatic intermittent titration technique (GITT) and DFT calculations. Furthermore, ex situ X-ray photoelectron spectroscopy (XPS), transmission electron microscopy (TEM), and X-ray diffraction (XRD) were carried out to reveal the detailed ion storage mechanism.

2. Experimental

2.1. Preparation of Nb_2O_5@rGO

Firstly, 2.5 mmol $C_{10}H_5NbO_{20}{\cdot}xH_2O$ was slowly added to 35 mL distilled water under continuous stirring for 2 h to prepare a clear solution. Afterward, a specific amount of GO (2 mg mL^{-1}, provided by XFNANO company) was slowly dropped into the above solution. Then, the well-dispersed suspensions were spray-dried through the B-290 Buchi mini spray dryer to obtain Nb_xO_y@GO composite. Finally, the prepared Nb_xO_y@GO composite was calcinated at 300 °C for 1 h and then at 500, 700, and 900 °C for 3 h at a rate of 2 °C min^{-1} in an Ar atmosphere. After calcination at different temperatures, GO was reduced to rGO and the highly crystallized Nb_2O_5 is synthesized [28–31]. In addition, the pure rGO was also prepared at the same conditions.

2.2. Materials characterization

Scanning electron microscope (SEM) images and energy dispersive spectrometry (EDS) elemental mappings were recorded using the JEOL-7100F microscope. TEM, high-resolution TEM (HRTEM), and high-angle annular dark-field (HAADF) images were collected by a JEM-2100F STEM/EDS microscope. XRD patterns were acquired using the D8 Advance X-ray diffractometer with a Cu K_α X-ray source. XPS experimental details were obtained via the VG MultiLab 2000 instrument. Raman spectra were recorded through the HORIBA LabRAM micro-Raman spectrometer. Thermogravimetric analyzer (TGA) was performed on a Netzsch STA-449C thermobalance with a temperature ramp of 5 °C min^{-1} under an air gas.

All calculations discussed here were performed using the CASTEP code in Materials Studio (version 2017 R2) of Accelrys Inc. Perdew-Burke-Ernzerhof (PBE) generalized gradient approximation (GGA) was carried out for the electronic exchange–correlation function. The energy cutoff for the projected-augmented plane-wave method was chosen to 600 eV. Brillouin zone sampling was set to 2 2 4. Energy difference for SCF tolerance was set to 1.0×10^{-6} eV/atom for reaching accurate electronic ground-state. The maximum force tolerance was set to 0.05 eV/Å for structural relaxation. Transition search method with complete LST/QST protocol was carried out for approximation of ion migration.

2.3. Electrochemical measurements

The cathode electrode was made through the simple mix of 70 wt% as-synthesized active materials, 20 wt% acetylene black, and 10 wt% polytetrafluoroethylene (PTFE). The mass loading of Nb_2O_5@rGO was about 2.5 mg cm^{-2}. All the capacities are calculated based on the mass of Nb_2O_5@rGO. With activated carbon (AC) as the anode (~2.4 V vs. Mg^{2+}/Mg), 0.3 M $Mg(TFSI)_2$ dissolved in DME as the electrolyte, the 2016 coin cells were assembled using glass fiber as the separator to characterize Mg-ion storage performance [3]. The Mg^{2+}/Li^+ hybrid ion batteries were assembled by using the obtained cathode, Mg metal anode in all-phenyl-complex (APC) electrolyte with LiCl (1 M) addition as Li source [32]. The electrochemical performance of pure rGO (annealed at 700 and 900 °C) was also obtained. The charge/discharge cycles and GITT measurements were performed on the cells by using the battery test system (LAND CT2001A). The GITT is conducted at the current density of 20 mA g^{-1} with a constant current pulse time of 30 min followed by a pause of 10 min [32,33]. Electrochemical impedance spectra (EIS) were conducted at the open-circuit condition. The frequency ranges from 10^{-2} to 10^5 Hz with the sinus amplitude of 10 mV on the VMP-3 multichannel electrochemical workstation. Cyclic voltammetry (CV) tests were conducted on the VMP-3 multichannel electrochemical workstation at different scan rates from 0.1 to 2 mV s^{-1}.

3. Results and discussion

During the spray-drying process, the moisture is rapidly evaporated and the ultrafine powder products were collected. The composite has a spherical morphology (Fig. S1a, b) with the diameter from several hundred nanometers to several micrometers. The spheres display a smooth surface without any grown particles. The EDS elemental mappings (Fig. S1c) demonstrate that every element matches well with the Nb_xO_y@GO composite. In order to obtain highly crystallized Nb_2O_5@rGO with different phase structures, the precursor was annealed at different temperatures, namely 500, 700, and 900 °C. As shown in Fig. 1(a), XRD patterns of the samples were firstly illustrated. The sample obtained at 500 °C displays several broad peaks with low intensity, indicating that Nb_xO_y@rGO existed in a poorly crystallized form. With the temperature increased to 700 °C and 900 °C, two different crystallographic systems of TT-Nb_2O_5@rGO and T-Nb_2O_5@rGO are formed with high purities [21,34]. The crystal structures of the two phases are clearly shown in Fig. S2. The two phases have similar structures, and the structure of TT-Nb_2O_5 is regarded as a disordering modification of T-Nb_2O_5 [34,35]. Fig. 1(b) displays the XPS spectra of Nb 3d peaks located at 209.64 and 206.89 eV, which belong to Nb $3d_{5/2}$ and Nb $3d_{3/2}$ of Nb^{5+}, demonstrating the formation of Nb_2O_5 in the two phases [22,36]. Raman spectra are collected to study the existed bands in the two phases (Fig. 1c). The characteristic bands located at 550–800 cm^{-1} and 200–400 cm^{-1} are ascribed to the high-wavenumber bands group (V_{Hi}) and mid-wavenumber bands group (VM_{id}) of Nb_2O_5 [21]. Two broadened bands located at about 1345 and 1590 cm^{-1} are corresponding to

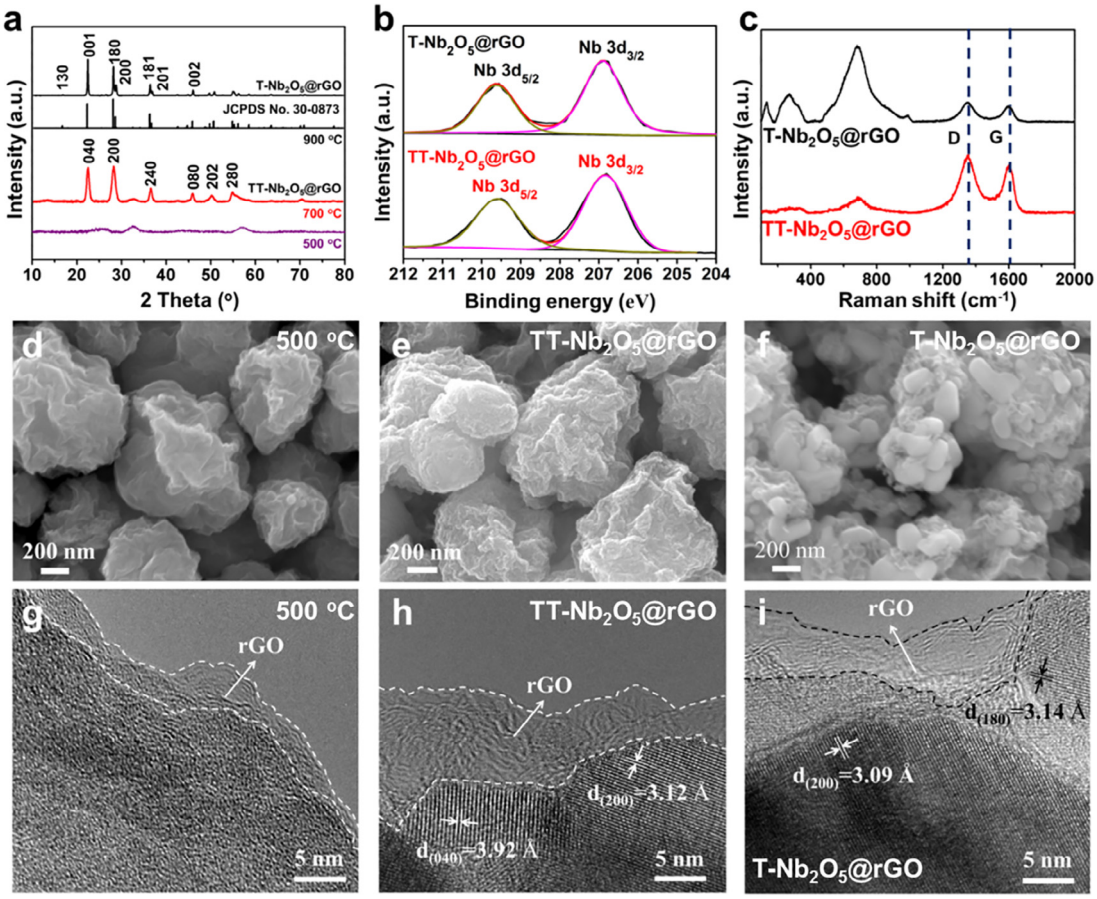

Fig. 1. (a) XRD patterns of Nb_2O_5 with different polymorphs. (b) XPS of Nb 3d and (c) Raman spectra of TT-Nb_2O_5@rGO and T-Nb_2O_5@rGO. SEM images (d–f) and HRTEM images (g–i) of the obtained samples after annealing at 500 °C (d and g), 700 °C (e, h) and 900 °C (f and i).

D-band and G-band (graphite). Besides, the calculated I_D/I_G of TT-Nb_2O_5@rGO and T-Nb_2O_5@rGO is 1.17 and 1.23, indicating a negligible difference in the graphitization degree of carbon. The TGA results (Fig. S3) also revealed a similar carbon content in TT-Nb_2O_5@rGO (3.68%) and T-Nb_2O_5@rGO (3.75%). The Raman and TGA results indicate that there is not much difference in carbon graphitization degree and carbon content between the two phases. Furthermore, the electrochemical performance of pure rGO (under two annealing conditions of 700 and 900 °C) for Mg-storage and Li-storage was also obtained. As shown in Fig. S4, both of the pure rGO display poor electrochemical performance and show no obvious difference. Based on these results, it can be reasonably speculated that the difference of rGO in the composite obtained at different temperatures should be ignored.

The morphologies of the synthesized samples were analyzed by SEM and TEM. As presented in Fig. 1d, e, f and Fig. S5a, b, c, the samples prepared at 500, 700 and 900 °C show a similar spherical morphology supported by three-dimensional rGO frameworks with the diameter from 100 nm to 2 μm. The elemental mappings of the three samples (Fig. S5d–f) show the uniform distribution of Nb, O and C in the product, indicating the formation of Nb_xO_y@rGO composite. The sample annealed at 500 °C has a smooth folded rGO surface without obvious wrapped Nb_xO_y particles (Fig. S6a, d, g). The HRTEM image in Fig. 1g displays no lattice fringes, demonstrating the uncrystallized structure, which is corresponding well with the XRD result (Fig. 1a). With the temperature increased to 700 °C (TT-Nb_2O_5@rGO), the ultrafine Nb_2O_5 nanoparticles (about 30 nm) are well-distributed in rGO frameworks (Fig. S6b, e, h). Fig. 1h shows clear lattice spacing of 3.92 and 3.12 Å, which is consistent with the (040) and (200) planes of TT-Nb_2O_5. The particle size of Nb_2O_5 is about 200 nm (Fig. S6c, f, i) when annealed at 900 °C (T-Nb_2O_5@rGO). The interlayer spacings (Fig. 1i) of 3.14 and 3.07 Å are ascribed to the (180) and (200) lattice planes of T-Nb_2O_5. The HRTEM image (Fig. 1i) also shows the good combination of Nb_2O_5 nanoparticles with the amorphous graphene network. The SEM images of pure rGO annealing at 700 °C (Fig. S7a and b) and 900 (Fig. S7c and d) °C clearly show the rGO framework. Furthermore, the elemental mappings images of TT-Nb_2O_5@rGO (Fig. S7e) and T-Nb_2O_5@rGO (Fig. S7f) after etching with HF shows only the carbon skeleton and C element, demonstrating the rGO supporting framework in the composite. When used as electrode materials, the nanometer-sized Nb_2O_5 has a small particle size and a high surface area, leading to low thermodynamic stability and high activity, which are harmful to the electrochemical performance. The construction of the nano hierarchical structure of Nb_2O_5@rGO is an effective method to avoid the side effect of nanomaterials [37]. Moreover, the three-dimensional graphene network can avoid the agglomeration of Nb_2O_5 nanoparticles and provide good conductivity, facile ion/electron transport, and high electrode–electrolyte interface area, which are beneficial to the electrochemical performance.

The Mg storage performance was first investigated on a cell configuration based on Nb_2O_5 cathode, AC counter electrode, and $Mg(TFSI)_2$/DME electrolyte. Fig. 2(a) displays the charge and discharge profiles of TT-Nb_2O_5@rGO and T-Nb_2O_5@rGO in the potential region between 0.9 and 3.6 V vs. Mg^{2+}/Mg at 0.05 A g^{-1}. Both the two phases exhibit a discharge plateau at around 1.1 V (vs. Mg^{2+}/Mg) and a charge plateau at around 1.3 V (vs. Mg^{2+}/Mg).

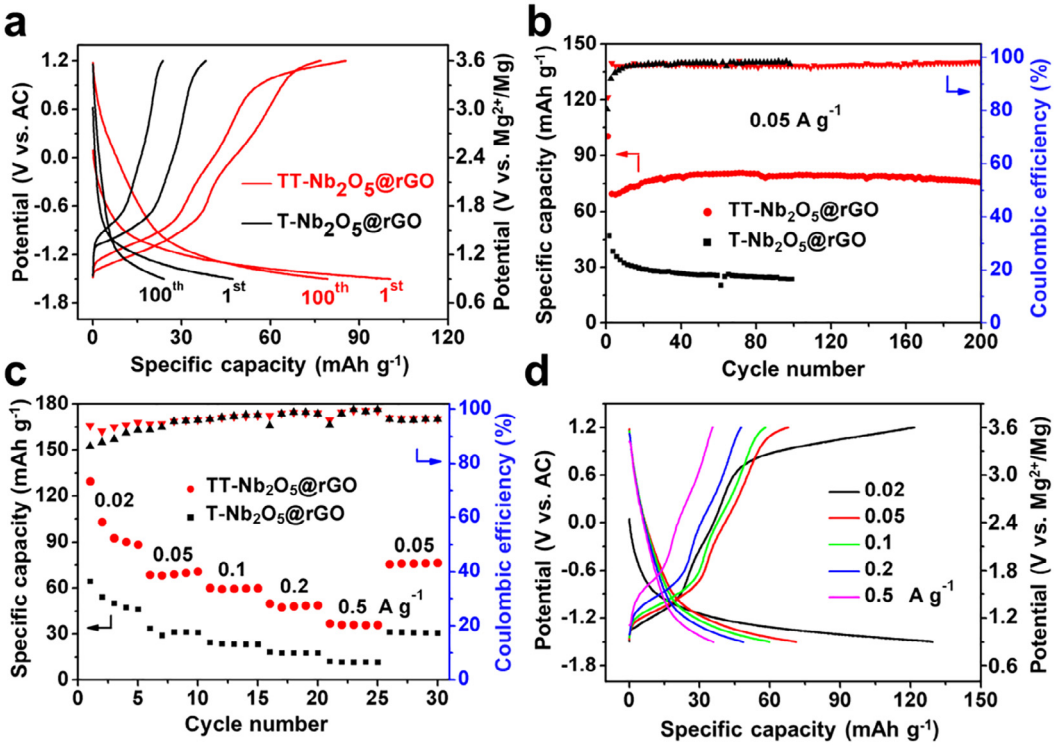

Fig. 2. Electrochemical performance of TT-Nb_2O_5@rGO and T-Nb_2O_5@rGO for Mg-storage. (a) The discharge–charge curves and (b) cycling performance at 0.05 A g^{-1}. (c) Rate performance. (d) Discharge-charge profiles of TT-Nb_2O_5@rGO at various rates.

The slope plateau above 3.2 V (vs. Mg^{2+}/Mg) in the charging process may be caused by side reactions, and the sloping plateau disappeared in the following cycles. However, TT-Nb_2O_5@rGO has a higher discharge capacity (100.4 mAh g^{-1}) compared with T-Nb_2O_5@rGO (47.3 mAh g^{-1}). Obviously, TT-Nb_2O_5@rGO also exhibits better cycling stability and higher reversible discharge capacity (Fig. 2b). At the current density of 0.05 A g^{-1}, TT-Nb_2O_5@rGO exhibited high capacities of 79.3 and 75.5 mAh g^{-1} after 100 and 200 cycles, respectively. For T-Nb_2O_5@rGO, only a much lower capacity of 24.1 mAh g^{-1} is maintained after 100 cycles. The cycle and rate capability of the two samples were also examined and displayed in Fig. 2(c). In general, TT-Nb_2O_5@rGO shows a much better rate performance than that of T-Nb_2O_5@rGO. As for TT-Nb_2O_5@rGO, the discharge capacities with increased current densities from 0.02 to 0.5 were 129.5, 68.4, 59.8, 49.7 and 36.7 mAh g^{-1}, respectively. For T-Nb_2O_5@rGO, the capacities are much lower at the same rates. In addition, TT-Nb_2O_5@rGO shows higher coulombic efficiency in the first several cycles than T-Nb_2O_5@rGO (Fig. 2b, c), revealing better reversible capability of TT-Nb_2O_5@rGO. Fig. 2(d) illustrates the corresponding discharge and charge profiles of TT-Nb_2O_5@rGO at various rates. All of the discharge curves show similar profiles, however, the polarization phenomenon becomes obvious at high current densities.

Mg^{2+}/Li^+ hybrid ion batteries were also assembled to further study the Li-ion storage performance of TT-Nb_2O_5@rGO and T-Nb_2O_5@rGO. Fig. 3(a) shows the discharge-charge process of the two phases between 0.5 and 2 V (vs. Mg^{2+}/Mg) at 0.1 A g^{-1}, the capacity is 153.4 and 119.7 mAh g^{-1} for T-Nb_2O_5@rGO and TT-Nb_2O_5@rGO, respectively. Although the capacity is lower than the reported two-dimensional Nb_2O_5 holey nanosheets (195.9 mAh g^{-1}, over a larger operating voltage range of 0.2–1.8 V vs. Mg^{2+}/Mg), both samples show an obvious plateau at about 0.9 V vs. Mg^{2+}/Mg (Fig. 3a) [38]. Furthermore, the two phases displayed excellent cycling stability and enhanced rate performance. The capacity of 134.3 and 103.9 mAh g^{-1} is obtained for T-Nb_2O_5@rGO and TT-Nb_2O_5@rGO even after 200 cycles (Fig. 3b), the retention of the capacity is 87.5% and 86.8% (much higher than Nb_2O_5 holey nanosheets of 70% at 0.2 A g^{-1} after 100 cycles), respectively. More importantly, T-Nb_2O_5@rGO displays an enhanced rate performance (Fig. 3c) with the reversible capacities of 162, 155.6, 149.2, 138.7, 126.2, and 114.8 mAh g^{-1} when the current densities increased from 0.05 to 2 A g^{-1}. Even at the extremely high current densities of 4 and 8 A g^{-1}, the discharge capacity of 97.1 and 61.5 mAh g^{-1} is still maintained, which is much better than the Nb_2O_5 holey nanosheets (72.1 mAh g^{-1} at 2 A g^{-1}) [38]. When turned back to 0.1 A g^{-1}, the capacity recovered back to 150.9 and 106.8 mAh g^{-1}, showing high reversibility. The charge–discharge curves of T-Nb_2O_5@rGO exhibit slope plateau at various current densities and the polarization phenomenon become obvious with the increase of current densities (Fig. S8). At all the same current densities, TT-Nb_2O_5@rGO exhibits much lower discharge capacity compared with that of T-Nb_2O_5@rGO, as reported in the LIBs [21,23,27]. In addition to the effect of Nb_2O_5 nanoparticle sizes, to select a suitable phase of Nb_2O_5 is a practical strategy to significantly improve the electrochemical performance. In order to reveal the difference between T-Nb_2O_5@rGO and TT-Nb_2O_5@rGO in the hybrid system, the kinetics of Li^+ solid-state diffusion was studied by GITT [33]. As shown in Fig. S9, T-Nb_2O_5@rGO and TT-Nb_2O_5@rGO exhibit a much higher specific capacity of 186.7 (Fig. S9b) and 140.9 mAh g^{-1} (Fig. S9a) in GITT measurements. Furthermore, T-Nb_2O_5@rGO displays a little faster Li^+ diffusivity during the entire intercalation process (Fig. 3d). The calculated specific average diffusivity is 1.62×10^{-11} and 1.31×10^{-11} cm^2 s^{-1} for T-Nb_2O_5@rGO and TT-Nb_2O_5@rGO, respectively. T-Nb_2O_5@rGO also exhibits excellent cycling stability at a high current density of 2 A g^{-1} (Fig. 3e). The cell was activated at 0.1 A g^{-1} for 5 cycles prior to allowing full contact of Nb_2O_5 nanoparticles with electrolytes. After the activation process, the

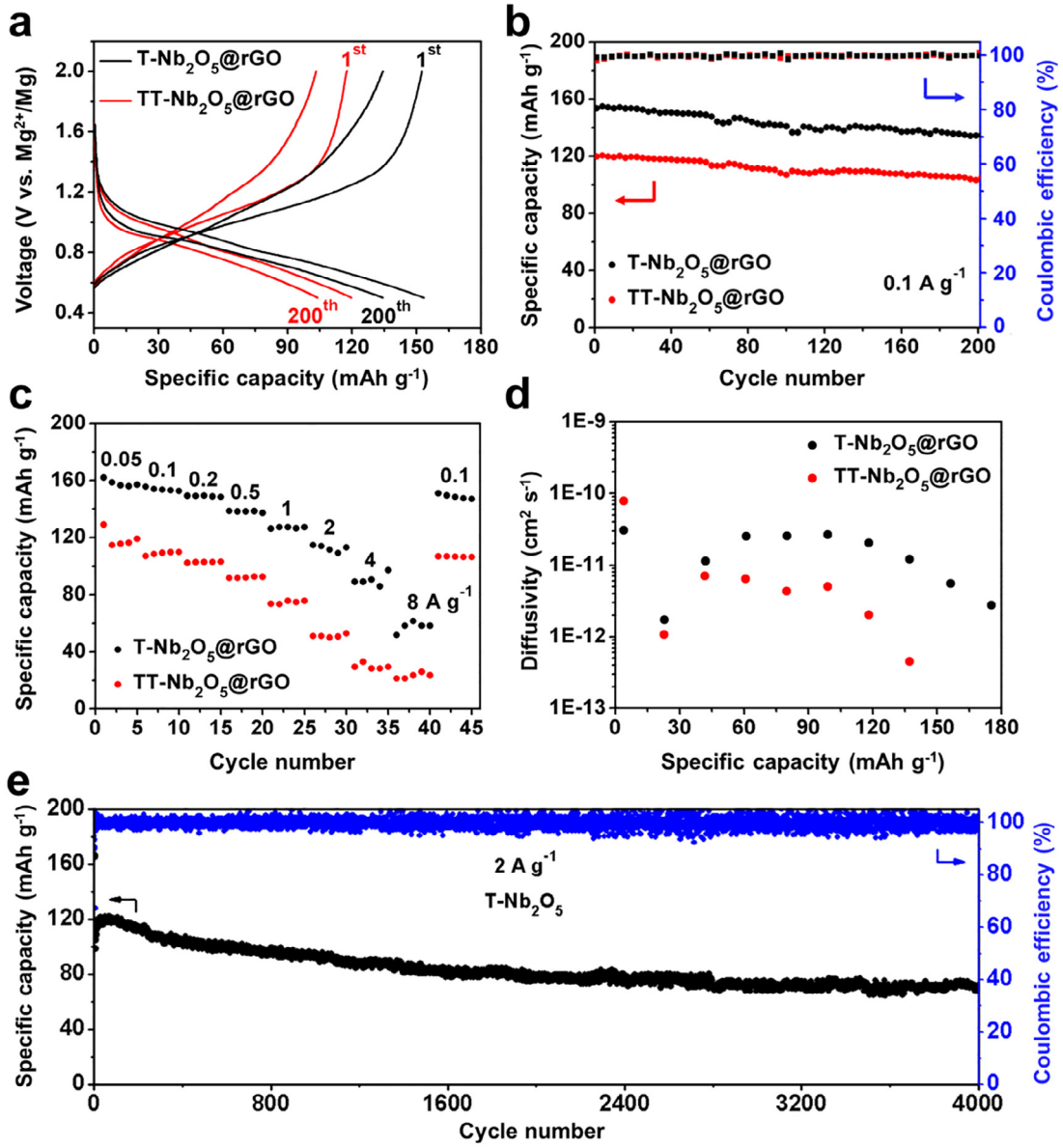

Fig. 3. Electrochemical performance of TT-Nb_2O_5@rGO and T-Nb_2O_5@rGO in Mg^{2+}/Li^+ hybrid ion batteries. (a) Galvanostatic discharge–charge profiles and (b) cycling performance of TT-Nb_2O_5@rGO and T-Nb_2O_5@rGO at the current density of 0.1 A g^{-1}. (c) Rate capability. (d) Li^+ diffusivity versus the state of discharge. (e) Cycling stability of T-Nb_2O_5@rGO at a high current density of 2 A g^{-1}.

discharge capacity is 98.5 mAh g^{-1} and slowly increased to 120.6 mAh g^{-1} within 20 cycles. The capacities of 95.9, 77.3, 73.1, and 72.5 mAh g^{-1} are retained after 1000, 2000, 3000, and 4000 cycles, corresponding to 79.5%, 64.1%, 60.5% and 60.1% capacity retention of the highest capacity during cycling. The three-dimensional rGO network wrapped Nb_2O_5 nanoparticles provides high conductivity and structural stability, which contribute greatly to the outstanding rate capability and superior cycling stability.

The Li-ion storage performance and corresponding reaction mechanism of TT-Nb_2O_5 and T-Nb_2O_5 in LIBs were extensively investigated in previous papers [21,24,39]. On the Nb_2O_5 electrode side, Mg^{2+}/Li^+ hybrid batteries have a similar electrochemical reaction mechanism with that of LIBs [38]. Therefore, Nb_2O_5 is supposed to undertake a Li^+ intercalation/deintercalation mechanism in hybrid batteries. Based on the experimental and theoretical analysis, there is not much difference in Li^+ diffusivity (1.62×10^{-11} and 1.31×10^{-11} cm^2 s^{-1}) and migration energy (0.47 and 0.46 eV) for T-Nb_2O_5 and TT-Nb_2O_5 [21]. However, T-Nb_2O_5 possesses more lithium storage sites and shorter Li diffusion distance, which are beneficial to the higher specific capacity and better rate capability, as demonstrated in our work [21].

In order to investigate the magnesiation and demagnesiation of reaction, we performed the ex situ HRTEM, XRD, and XPS for TT-Nb_2O_5@rGO at different states. Firstly, the HAADF image and EDS elemental mappings of TT-Nb_2O_5@rGO in the fully discharged state were collected. Fig. 4(a) presents the existence and uniform distribution of the Mg element in the structure, which indicates the successful magnesiation of TT-Nb_2O_5@rGO during the discharge process. As revealed in the HRTEM image (Fig. 4b), the (040) plane is expanded to 4.12 Å at a discharged state, corresponding well with the XRD result (Fig. 4c). Furthermore, the ex situ XRD results (Fig. 4c) display the reversible shift of (040) plane during discharge and charge, indicating the reversible intercalation mechanism for Mg storage. In addition, CV measurements at different sweeping

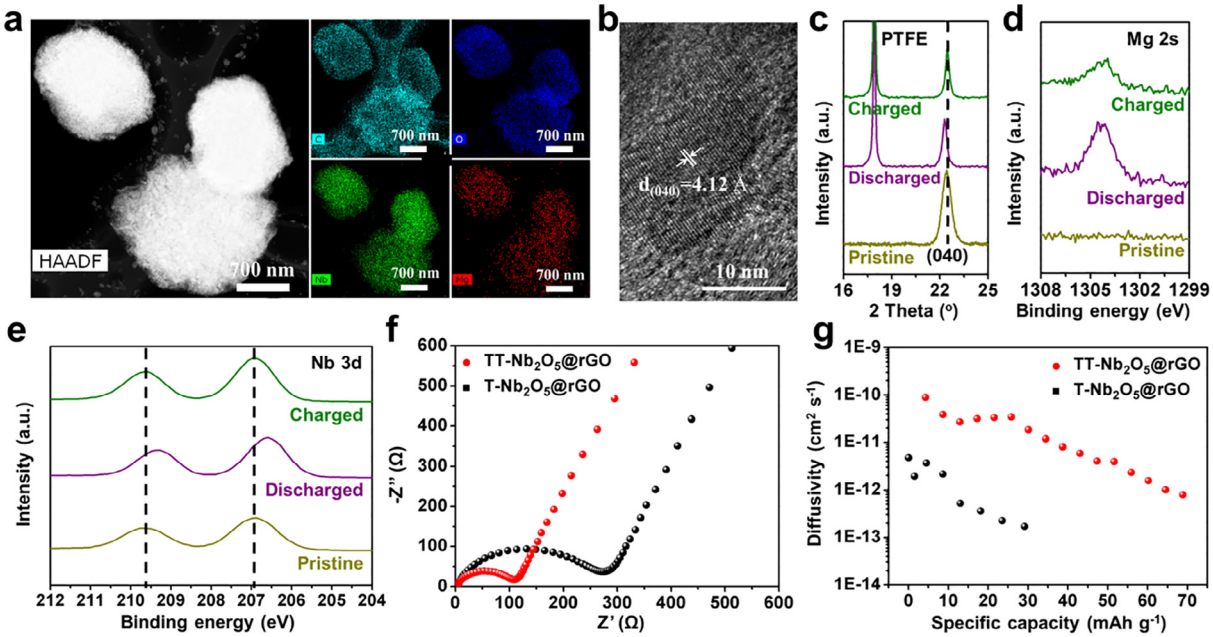

Fig. 4. (a) HAADF image and EDS elemental mappings of TT-Nb_2O_5@rGO at discharge state. (b) HRTEM image of TT-Nb_2O_5@rGO at discharge state. (c) Ex situ XRD, (d) XPS spectra of Mg 2s and (e) Nb 3d of TT-Nb_2O_5@rGO at different states. (f) Nyquist plots and (g) Mg^{2+} diffusivity of TT-Nb_2O_5@rGO and T-Nb_2O_5@rGO.

rates (0.1 to 2 mV s^{-1}) were performed to evaluate the Mg^{2+} intercalation kinetics of TT-Nb_2O_5@rGO (Fig. S10a). The currents of anodic peaks (centered at −0.8 V vs. AC) enhance while the locations shift as the scan rate increases. While no obvious cathodic peaks displayed in the discharging process, the peaks located at −1.5 V vs. AC were adopted to calculate the *b* value. As shown in Fig. S10b, the *b* values are very close to 0.5, demonstrating that the kinetics of Mg^{2+} migration is controlled by the diffusion process.[36,40,41] XPS spectra of Mg 2s and Nb 3d were also conducted on pristine, discharged and charged TT-Nb_2O_5@rGO to study the change of composition and chemical valence. The intensity of Mg 2s band at the discharged state is much higher than that of the charged state (Fig. 4d), demonstrating the insertion of Mg^{2+} at the discharged state and partially retention of Mg^{2+} at the charged state. The peak of Nb 3d shifted to lower binding energy at the discharged state and recovered to the original position at charged state (Fig. 4e), indicating the reversible oxidation and reduction reaction of Nb^{5+}. To further investigate Mg^{2+} diffusion kinetics in the host structures, EIS (Fig. 4f) and GITT (Fig. S11) were performed. TT-Nb_2O_5@rGO shows a much smaller semicircle in the high-frequency regions than that of T-Nb_2O_5@rGO, indicating a smaller charge-transfer resistance at TT-Nb_2O_5@rGO/electrolyte interface. More importantly, TT-Nb_2O_5@rGO exhibits about one order of magnitude faster of Mg^{2+} solid-state diffusion kinetics than T-Nb_2O_5@rGO (Fig. 4g). The calculated average Mg^{2+} diffusivity of TT-Nb_2O_5@rGO and T-Nb_2O_5@rGO is about 1.89×10^{-11} and

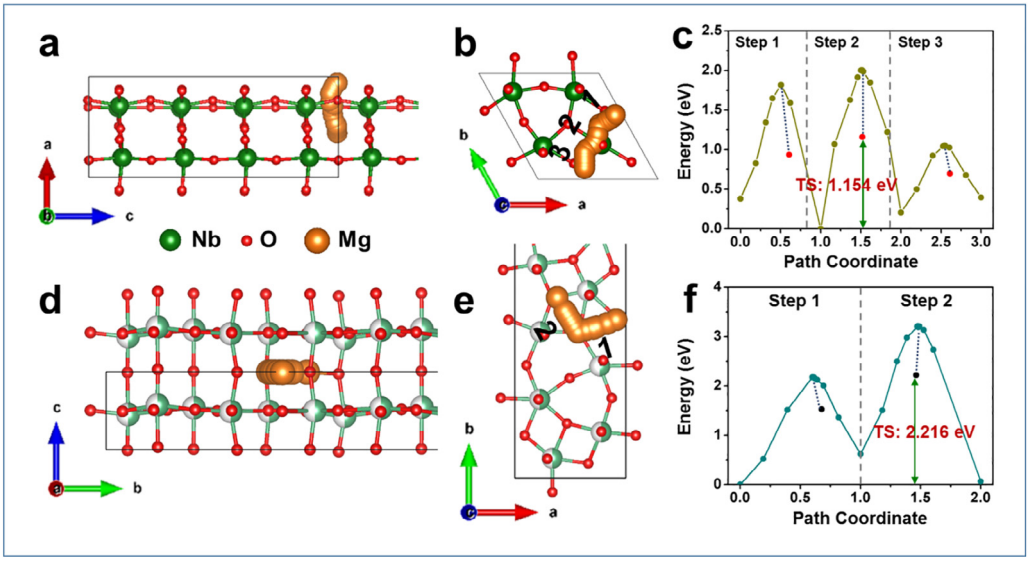

Fig. 5. Mg^{2+} migration routine in (a and b) TT-Nb_2O_5@rGO and (d and e) T-Nb_2O_5@rGO viewed from different lattice planes. (c and f) Diffusion energy barrier profiles of TT-Nb_2O_5@rGO and T-Nb_2O_5@rGO, respectively.

2.35×10^{-12} cm^2 s^{-1} during the discharge process. The EIS and GITT results provide direct evidence for the faster Mg^{2+} diffusion kinetics in TT-Nb_2O_5@rGO than that of T-Nb_2O_5@rGO, which is beneficial to the Mg-storage performance.

DFT calculations were also conducted to give a clear understanding of Mg^{2+} migration behavior during the insertion process. Based on the previous work [21,23], we simulated the most reasonable diffusion route for Mg^{2+} and calculated the corresponding energy profile along the migration path. The Mg-diffusion pathways in the structure involve the conventional vacancy hopping between adjacent positions. According to the results viewed from different lattice planes, we can conclude that the Mg^{2+} diffusion pathway is parallel to the *a*-axis in TT-Nb_2O_5 (Fig. 5a, b) and parallel to the *b*-axis in T-Nb_2O_5 (Fig. 5d, e), indicating fast Mg^{2+} diffusivity within the *ab* plane [21]. As shown in Fig. 5(c), the Mg^{2+} diffusion in TT-Nb_2O_5 displays the energy barrier of 0.931, 1.154, and 0.690 eV in three steps, respectively. Whereas, the Mg^{2+} diffusion in T-Nb_2O_5 is 1.525 and 2.216 eV in the two steps (Fig. 5f). To realize the successful migration of Mg^{2+}, the energy barrier of TT-Nb_2O_5 is 1.154 eV, which is much lower than that of T-Nb_2O_5 (2.216 eV). Therefore, TT-Nb_2O_5 displays much better Mg-ion storage performance. However, when compared with that of Li^+ (0.46 eV) [21], the activation energy of Mg^{2+} in the TT-Nb_2O_5 structure is much larger, indicating that the divalent Mg^{2+} interacts much stronger with the framework of TT-Nb_2O_5.

4. Conclusions

In summary, the three-dimensional graphene network-assisted different crystal structures of Nb_2O_5 (TT-Nb_2O_5, T-Nb_2O_5) nanoparticles were designed and constructed through a scalable spray-drying method. The two phases exhibit different electrochemical performance for Mg-ion and Li-ion storage, that is to say, TT-Nb_2O_5 displays much better Mg storage performance in $Mg(TFSI)_2$/DME electrolyte and T-Nb_2O_5 displays much better Li storage performance in APC-LiCl electrolyte. The ex situ TEM, XRD, and XPS results confirm the reversible Mg-ion intercalation reaction mechanism for TT-Nb_2O_5. Furthermore, experimental and computational investigations revealed the different crystal structure effects on Mg^{2+} and Li^+ diffusion kinetics. Our work demonstrates the importance of the exploration of materials space, especially for a specific structure that can provide a unique advantage for different ions storage.

Declaration of Competing Interest

The authors declare that they have no known competing financial interests or personal relationships that could have appeared to influence the work reported in this paper.

Acknowledgments

This work was supported by the National Natural Science Foundation of China (51972259, 51832004, 51521001), the Fundamental Research Funds for the Central Universities (WUT: 2020III043GX, 2020III015GX), Foshan Xianhu Laboratory of the Advanced Energy Science and Technology Guangdong Laboratory (XHT2020-003), the National Key Research and Development Program of China (2016YFA0202601), the Hubei Provincial Natural Science Foundation of China (2019CFB519).

Appendix A. Supplementary data

Supplementary data to this article can be found online at https://doi.org/10.1016/j.jechem.2020.10.033.

References

[1] P. Albertus, S. Babinec, S. Litzelman, A. Newman, Nat. Energy 3 (2017) 16–21.
[2] G. Hou, B. Cheng, Y. Yang, Y. Du, Y. Zhang, B. Li, J. He, Y. Zhou, D. Yi, N. Zhao, Y. Bando, D. Golberg, J. Yao, X. Wang, F. Yuan, ACS Nano 13 (2019) 10179–10190.
[3] Y. Xu, X. Deng, Q. Li, G. Zhang, F. Xiong, S. Tan, Q. Wei, J. Lu, J. Li, Q. An, L. Mai, Chem 5 (2019) 1194–1209.
[4] Y. Liang, H. Dong, D. Aurbach, Y. Yao, Nat. Energy (2020), https://doi.org/10.1038/s41560-41020-40655-41560.
[5] J. Muldoon, C.B. Bucur, T. Gregory, Chem. Rev. 114 (2014) 11683–11720.
[6] X. Xue, R. Chen, C. Yan, P. Zhao, Y. Hu, W. Kong, H. Lin, L. Wang, Z. Jin, Adv. Energy Mater. 9 (2019) 1900145.
[7] B. Li, R. Masse, C. Liu, Y. Hu, W. Li, G. Zhang, G. Cao, Energy Storage Mater. 22 (2019) 96–104.
[8] Q. Zhang, E. Takeuchi, J. Takeuchi, A. Marschilok, ECS Trans. 66 (2015) 171–181.
[9] X. Cheng, Z. Zhang, Q. Kong, Q. Zhang, T. Wang, S. Dong, L. Gu, X. Wang, J. Ma, P. Han, H.-J. Lin, C.-T. Chen, G. Cui, Angew. Chem. Int. Ed. (2020), https://doi.org/10.1002/anie.202002177.
[10] X.Q. Sun, P. Bonnick, L.F. Nazar, ACS Energy Lett. 1 (2016) 297–301.
[11] X. Sun, P. Bonnick, V. Duffort, M. Liu, Z. Rong, K.A. Persson, G. Ceder, L.F. Nazar, Energy Environ. Sci. 9 (2016) 2273–2277.
[12] P. Canepa, G. Sai Gautam, D.C. Hannah, R. Malik, M. Liu, K.G. Gallagher, K.A. Persson, G. Ceder, Chem. Rev. 117 (2017) 4287–4341.
[13] G. Gershinsky, H.D. Yoo, Y. Gofer, D. Aurbach, Langmuir 29 (2013) 10964–10972.
[14] G. Sai Gautam, P. Canepa, A. Abdellahi, A. Urban, R. Malik, G. Ceder, Chem. Mater. 27 (2015) 3733–3742.
[15] A. Mukherjee, N. Sa, P.J. Phillips, A. Burrell, J. Vaughey, R.F. Klie, Chem. Mater. 29 (2017) 2218–2226.
[16] A. Parija, Y.F. Liang, J.L. Andrews, L.R. De Jesus, D. Prendergast, S. Banerjee, Chem. Mater. 28 (2016) 5611–5620.
[17] T.M. Tolhurst, B. Leedahl, J.L. Andrews, P.M. Marley, S. Banerjee, A. Moewes, Phys. Chem. Chem. Phys. 18 (2016) 15798–15806.
[18] G.S. Gautam, P. Canepa, R. Malik, M. Liu, K.A. Persson, G. Ceder, Chem. Commun. 51 (2015) 13619–13622.
[19] M. Mao, T. Gao, S. Hou, C. Wang, Chem. Soc. Rev. 47 (2018) 8804–8841.
[20] S. Fu, Q. Yu, Z. Liu, P. Hu, Q. Chen, S. Feng, L. Mai, L. Zhou, J. Mater. Chem. A 7 (2019) 11234–11240.
[21] J. Meng, Q. He, L. Xu, X. Zhang, F. Liu, X. Wang, Q. Li, X. Xu, G. Zhang, C. Niu, Z. Xiao, Z. Liu, Z. Zhu, Y. Zhao, L. Mai, Adv. Energy Mater. 9 (2019) 1802695.
[22] L. Yang, Y.-E. Zhu, J. Sheng, F. Li, B. Tang, Y. Zhang, Z. Zhou, Small 13 (2017) 1702588.
[23] D. Chen, J.-H. Wang, T.-F. Chou, B. Zhao, M.A. El-Sayed, M. Liu, J. Am. Chem. Soc. 139 (2017) 7071–7081.
[24] B. Deng, T. Lei, W. Zhu, L. Xiao, J. Liu, Adv. Funct. Mater. 28 (2018) 1704330.
[25] H. Li, Y. Zhu, S. Dong, L. Shen, Z. Chen, X. Zhang, G. Yu, Chem. Mater. 28 (2016) 5753–5760.
[26] L. Yan, G. Chen, S. Sarker, S. Richins, H. Wang, W. Xu, X. Rui, H. Luo, ACS Appl. Mater. Interfaces 8 (2016) 22213–22219.
[27] V. Augustyn, J. Come, M.A. Lowe, J.W. Kim, P.-L. Taberna, S.H. Tolbert, H.D. Abruña, P. Simon, B. Dunn, Nat. Mater. 12 (2013) 518–522.
[28] P. Zhang, Z. Li, S. Zhang, G. Shao, Energy Environ. Mater. 1 (2018) 5–12.
[29] A. Ganguly, S. Sharma, P. Papakonstantinou, J.W.J. Hamilton, J. Phys. Chem. C 115 (2011) 17009–17019.
[30] X. Zhao, Z. Zhaokarger, M. Fichtner, X. Shen, Angew. Chem. Int. Ed. 59 (2020) 5902–5949.
[31] S. Pei, H. Cheng, Carbon 50 (2012) 3210–3228.
[32] C. Pei, F. Xiong, J. Sheng, Y. Yin, S. Tan, D. Wang, C. Han, Q. An, L. Mai, ACS Appl. Mater. Interfaces 9 (2017) 17060–17066.
[33] Q.Y. An, Y.F. Li, H.D. Yoo, S. Chen, Q. Ru, L.Q. Mai, Y. Yao, Nano Energy 18 (2015) 265–272.
[34] N. Kumagai, Y. Koishikawa, S. Komaba, N. Koshiba, J. Electrochem. Soc. 146 (1999) 3203–3210.
[35] J. Come, V. Augustyn, J.W. Kim, P. Rozier, P.L. Taberna, P. Gogotsi, J.W. Long, B. Dunn, P. Simon, J. Electrochem. Soc. 161 (2014) A718–A725.
[36] Z. Hu, Q. He, Z. Liu, X. Liu, M. Qin, B. Wen, W. Shi, Y. Zhao, Q. Li, L. Mai, Sci. Bull. 65 (2020) 1154–1162.
[37] Y. Guo, J. Hu, L. Wan, Adv. Mater. 20 (2008) 2878–2887.
[38] H. Huang, G. Zhao, N. Zhang, K. Sun, Nanoscale 11 (2019) 16222–16227.
[39] K.J. Griffith, A.C. Forse, J.M. Griffin, C.P. Grey, J. Am. Chem. Soc. 138 (2016) 8888–8899.
[40] Y. Jiang, S. Tan, Q. Wei, J. Dong, Q. Li, F. Xiong, J. Sheng, Q. An, L. Mai, J. Mater. Chem. 6 (2018) 12259–12266.
[41] R. Sun, S. Liu, Q. Wei, J. Sheng, S. Zhu, Q. An, L. Mai, Small 13 (2017) 1701744.